Advances in Water Resources 203 (2025) 105015

Contents lists available at ScienceDirect

Advances in Water Resources

journal homepage: www.elsevier.com/locate/advwatres

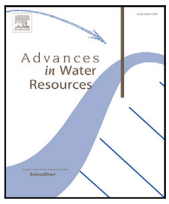

Dominant spatiotemporal structures in total water storage anomalies

G. Libero, V. Ciriello *

Department of Civil, Chemical, Environmental and Materials Engineering, University of Bologna, Italy

ARTICLE INFO

Keywords:
GRACE data
Dynamic mode decomposition
Reduced-order model
Hydrology
Dynamic process
Time series

ABSTRACT

This study employs Dynamic Mode Decomposition (DMD) to derive a global-scale linear model for the temporal evolution of Total Water Storage Anomaly (TWSA) measured by GRACE satellite missions, with the goal of extracting and analyzing the dominant spatiotemporal structures governing TWSA variability. Our analysis differentiates modes associated with a periodic dynamic – linked to precipitation-driven seasonal cycles and multi-year variations – from those incorporating trend effects indicating, on average, a progressive TWSA decline. Focusing on the latter, we examine patterns associated with extreme TWSA values and their intensification over time. In regions experiencing significant TWSA changes over the past decade, DMD effectively distinguishes natural variability from trends, aligning with previous findings that identify climate change and human impact effects in the same regions. This study underscores DMD's potential in capturing essential hydrological dynamics in data, thus supporting the interpretation of these dynamics at the scale of the analysis.

1. Introduction

Satellite missions yield environmental data with ever improving spatial coverage and temporal resolution, which is critical for studying large-scale hydrological process dynamics. The Gravity Recovery and Climate Experiment (GRACE) satellite mission and its successor, the GRACE follow-on (GRACE-FO) (Tapley et al., 2004; Landerer et al., 2020), measure Earth's gravity field variations to detect total water storage anomalies (TWSA) on the planet. GRACE data enable one to identify clear trends in freshwater depletion across diverse regions (Rodell et al., 2018; Stampoulis et al., 2019; Frappart et al., 2019; Scanlon et al., 2023) and draw an integrated view on the complex interaction between human activities and hydrological systems, which is critical to design sustainable water management practices (Tapley et al., 2019; Rodell and Reager, 2023).

The vulnerability of water resources to depletion is evident in regions affected by intensive irrigation and in areas impacted by severe droughts (Famiglietti et al., 2011; Castle et al., 2014). These alterations in hydrological systems, and consequent freshwater losses and shifts in water availability, disrupt the balance of freshwater systems by decreasing groundwater reserves and connected surface water flows and affect ecosystems and food security by jeopardizing biodiversity and critical ecosystem services (de Graaf et al., 2019). Analyzing spatiotemporal patterns in global hydrological data that affect water resource availability is essential to identify the underlying mechanisms driving these changes and design effective mitigation strategies (Huggins et al., 2022; Scanlon et al., 2023).

Decoding the wealth of information contained in the GRACE dataset to extract meaningful spatiotemporal patterns requires the use of robust, data-driven tools grounded in solid mathematical principles. Dynamic Mode Decomposition (DMD) is a powerful and versatile data-driven technique for analyzing dynamical systems based on the singular value decomposition (SVD) (Kutz et al., 2016). Originally developed within the fields of applied mathematics and fluid dynamics (Schmid, 2010), DMD has also gained popularity since it has shown its connection with the Koopman operator (Rowley et al., 2009; Mezić, 2013). DMD has since found applications across diverse scientific disciplines, including physics, engineering, and biology (Tu et al., 2014; Kutz et al., 2016; Lu and Tartakovsky, 2020, 2021; Libero et al., 2024c). The method decomposes high-dimensional, time-dependent datasets into spatial modes paired with corresponding temporal dynamics, facilitating the identification of coherent structures and intrinsic dynamic behaviors within complex datasets. Ultimately, it enables reconstructing an optimal linear model mimicking the dynamic from these structures (Kutz et al., 2016).

As in Principal Component Analysis (PCA) and Empirical Orthogonal Functions (EOF)—which are mathematically equivalent techniques—DMD is a method for analyzing high-dimensional data, but it differs fundamentally in focus. PCA and EOF identify spatial patterns that capture the most variance in the data, producing orthogonal modes that are optimal for compression and noise reduction, but they do not account for time dynamics. In contrast, DMD captures the underlying

* Corresponding author.
E-mail address: v.ciriello@unibo.it (V. Ciriello).

https://doi.org/10.1016/j.advwatres.2025.105015
Received 4 March 2025; Received in revised form 15 May 2025; Accepted 16 May 2025
Available online 28 May 2025

temporal behavior by identifying modes associated with specific frequencies and growth or decay rates, making it well-suited for analyzing and forecasting dynamical systems (Kutz et al., 2016).

In Libero et al. (2024b), we investigate the capability of DMD to reproduce the dynamics of global-scale GRACE data, i.e., we use the method as a predictive tool. In particular, we focus on deriving the optimal linear operator within the DMD framework, which provides a linear approximation for advancing system states over time. We compare two different DMD algorithms and evaluate their performance in representation and extrapolation. The results reported in this study demonstrate that DMD facilitates data compression and enables extrapolation from a reduced set of spatially correlated structures with their associated dynamic. Moreover, we show that DMD maintains high predictive accuracy for global system dynamics while effectively reconstructing local time series.

Here, we do not use the method to make predictions, but we employ DMD to extract and analyze the dominant spatiotemporal structures in GRACE data. The objective is to leverage all available data during the training phase, focusing on identifying and interpreting key periodic and trend-dominated modes characteristic of the whole observation period. The approach reveals distinct patterns of water storage variability driven by these modes across different regions. By distinguishing the contributions in TWSA between natural cyclical fluctuations and long-term trends, we uncover the accelerating depletion of water resources in several critical areas. Our results highlight the increasing influence of trend-dominated modes over the observation period, particularly in regions affected by water depletion and climate-driven changes. This study demonstrates the capability of DMD to provide valuable insights into the global dynamics of water storage, offering a data-driven framework for monitoring and interpreting large-scale hydrological changes.

The paper is organized as follows. Section 2 is devoted to the presentation of both our methodological framework and Section 3 to the data used in the study. Section 4 reports the discussion of the results. Section 5 provides final remarks.

2. Materials and methods

We arrange the sequence of TWSA snapshots into column vectors, $\mathbf{x}_k = \mathbf{x}(t_k)$ with $\dim(\mathbf{x}_k) = N$, $t_k = k\Delta t$ and $k = 1, \dots, M$, i.e., M is the number of time points, while N denotes the number of spatial elements in the grid used for discretizing the snapshots. We do so to build two matrices, $\mathbf{X}, \mathbf{X}' \in \mathbb{R}^{N\times M}$ with $M \ll N$, so that for each column $\mathbf{x}_k$ in $\mathbf{X}$, the corresponding column in $\mathbf{X}'$ is one timestep Δt ahead in the future.

The DMD seeks to derive a linear approximation of the flow map of the nonlinear dynamic system as follows

$$\mathbf{X} \approx \mathbf{A}\mathbf{X}', \quad \mathbf{A} = \underset{\mathbf{A}}{\operatorname{argmin}} \|\mathbf{X}' - \mathbf{A}\mathbf{X}\|_F = \mathbf{X}'\mathbf{X}^{\dagger}, \tag{1}$$

where $\|.\|_F$ is the Frobenius norm and $\mathbf{A} \in \mathbb{R}^{N\times N}$. To reduce the computational cost of (1), the rank-r SVD – singular value decomposition – approximation $\mathbf{X} \approx \mathbf{U}\mathbf{\Sigma}\mathbf{V}^{\top}$, with $\mathbf{U} \in \mathbb{R}^{N\times r}$, $\mathbf{\Sigma} \in \mathbb{R}^{r\times r}$, $\mathbf{V} \in \mathbb{R}^{M\times r}$, is adopted. Then, one can obtain a low-dimensional linear model on POD coordinates as follows

$$\tilde{\mathbf{A}} = \mathbf{U}^{\top}\mathbf{A}\mathbf{U} = \mathbf{U}^{\top}\mathbf{X}'\mathbf{V}\mathbf{\Sigma}^{-1}, \tag{2}$$

where $\tilde{\mathbf{A}} \in \mathbb{R}^{r\times r}$. An approximation of the leading spectral decomposition of the original operator $\mathbf{A}$ is given by

$$\tilde{\mathbf{A}}\mathbf{W} = \mathbf{W}\mathbf{\Lambda}, \tag{3}$$

where the eigenvalues, $\lambda_1, \dots, \lambda_r$, stored in the diagonal matrix $\mathbf{\Lambda} \in \mathbb{R}^{r\times r}$ correspond to the eigenvalues of $\mathbf{A}$, while the eigenvectors, $\boldsymbol{\phi}_1, \dots, \boldsymbol{\phi}_r$, of $\mathbf{A}$, stored in the columns of $\mathbf{\Phi} \in \mathbb{R}^{N\times r}$, are computed as $\mathbf{\Phi} = \mathbf{X}'\mathbf{V}\mathbf{\Sigma}^{-1}\mathbf{W}$ (Kutz et al., 2016).

The eigenvectors of $\mathbf{A}$ are commonly named DMD *modes* and represent space-correlated structures, i.e., spatial patterns, that evolve in time according to the dynamic characteristics embedded in the eigenvalues. As such, each mode $\boldsymbol{\phi}_i$ is a vector with the same dimension as the vectorized snapshots and provides information about the cells in the domain where the mode is active. Specifically, each element in $\mathbf{\Phi}$ is usually a complex value, and the angle between the real and imaginary components represents the oscillation *phase* of that element relative to the others, i.e., a spatial shift. Furthermore, the absolute value of each matrix element corresponds to the *magnitude*, which is the spatial location's participation in that mode, with the same unit as the original data (Kutz et al., 2016).

The eigenvalues of $\mathbf{A}$, λ_i with $i = 1, \dots, r$, describe the dynamic behavior of the spatial patterns represented by the corresponding modes. Specifically, for each mode, a *time dynamic* can be determined as

$$\tau_i = \exp(\omega_i t), \tag{4}$$

where $\omega_i = \ln(\lambda_i)/\Delta t$ is the continuous-time counterpart of the eigenvalue λ_i. The DMD decomposition allows reconstruction of the system state evolution or even projection in the future as follows

$$\mathbf{x}(t) \approx \sum_{i=1}^{r} \boldsymbol{\phi}_i \tau_i b_i = \mathbf{\Phi}\mathbf{T}(\mathbf{\Lambda})\mathbf{b}. \tag{5}$$

where $\mathbf{T}$ is the matrix containing the time dynamics τ_i, and $\mathbf{b} = \mathbf{\Phi}^{\dagger}\mathbf{x}_1$ is the matrix of the corresponding amplitudes b_i that denote how much each mode contributes to the overall signal at the initial time (Kutz et al., 2016).

As discussed in the literature, the standard DMD framework (1) is affected by sensitivity to measurement noise, which may induce bias in the eigenvalue distribution and consequently affects the forecasting and reconstruction ability (Bagheri, 2014; Dawson et al., 2016; Hemati et al., 2017; Duke et al., 2011). Here, among the DMD algorithms that pursue the computation of the modes and time dynamics, we adopt the optimized DMD (optDMD) (Askham and Kutz, 2018) which is based on a variable projection method for nonlinear least squares to ease the decomposition of unevenly timed samples (Sashidhar and Kutz, 2022). Specifically, this algorithm is based on the direct solution of an exponential fitting problem as follows

$$\underset{\mathbf{\Lambda},\mathbf{\Phi},\mathbf{b}}{\operatorname{argmin}} \|\mathbf{X} - \mathbf{\Phi}\mathbf{T}(\mathbf{\Lambda})\mathbf{b}\|_F. \tag{6}$$

This formulation effectively suppresses bias and handles snapshots collected at arbitrary times, yielding modes and eigenvalues that are less sensitive to noise than those computed with standard DMD. However, these advantages come at the cost of solving a nonlinear, nonconvex optimization problem, which may fail to converge as the problem size increases. To mitigate this, the optDMD algorithm can be combined with statistical bagging methods to enhance robustness by stabilizing and cross-validating the DMD model through ensembling (Sashidhar and Kutz, 2022).

In the following, we define with TWSA_t the GRACE data at a give time t, while $\mathrm{TWSA}_t^{\mathcal{L}}$ is the correspondent prediction given by the linear model obtained with the optDMD algorithm truncated at $r = 10$ according to a criteria of data compression and based on error analysis (Libero et al., 2024a). The mode and time dynamics derived from GRACE data discussed in this paper include the periodic and trend components present in the dataset. However, our analysis is not unique since it depends on the algorithm choices and is referred to the selected time frame.

We evaluate the performance of the method by comparing observed and simulated system states. The difference between the state of the system predicted by the DMD model and the real snapshot at time t is defined as

$$\mathbf{d}_t^{\mathcal{L}} = \mathrm{TWSA}_t^{\mathcal{L}} - \mathrm{TWSA}_t. \tag{7}$$

3. Data

This analysis is based on the time series of monthly TWSA maps provided by the GRACE satellite mission (Tapley et al., 2004; Watkins et al., 2015), operational from April 2002 to October 2017, and its successor, GRACE-FO (Landerer et al., 2020), launched in 2018 and currently active. We employed the most recent GRACE mascon product (RL06.1Mv03) from the Jet Propulsion Laboratory archive (NASA/JPL, 2023), along with a 0.5-degree scaling factor map designed to reduce signal attenuation during sampling and post-processing (Wiese et al., 2016). This scaling enhances the native resolution of 3 degrees in both latitude and longitude. Since these scaling factors, optimized for reducing leakage errors in continental hydrology applications (Wiese et al., 2016), are not computed for ice-covered regions such as Greenland and Antarctica, these regions are excluded from our study.

The dataset includes $M = 232$ monthly global matrices of anomalies in centimeters of equivalent water thickness derived from satellite gravity field measurements, referenced to a baseline mean calculated from January 2004 to December 2009. The TWSA snapshot series spans from April 2002 ($t = 1$) to April 2024 ($t = 265$), with some short-term gaps and a major interruption during the transition between the two missions. Our analysis focuses on the evolution of TWSA across $N = 58\,908$ grid elements located in land areas. As explained in Section 2, in the data matrix, the columns represent different time points of TWSA data, and for each time point, the correspondent snapshot is flattened into a vector in a latitude-first order. This choice does not impact the results discussed later. Also, the presence of gaps is not an issue because, in the DMD framework, the data does not have to be sequential or uniformly sampled in time. DMD can be used to analyze the dynamics of a generic – not necessarily sequential – time series. The method requires the columns of $\mathbf{X}$ and $\mathbf{X}'$ to be related by the dynamics of interest. This means that only the pairwise correspondence between the columns of $\mathbf{X}$ and $\mathbf{X}'$ is relevant (Tu et al., 2014).

Although the analysis was conducted over 232 months of data, we have chosen to present the results as functions of t, where t represents time in months and ranges from 1 to 265, and to connect the results linearly across any gaps in the data.

4. Results and discussion

We apply DMD to derive a linear model for the temporal evolution of TWSA using the time series of snapshots provided by the GRACE satellite mission (see Sections 2, and 3). This linear model enables the identification of dominant spatiotemporal structures within the data. Specifically, DMD extracts a reduced set of modes that represent spatially correlated structures along with their temporal dynamics, as shown in Appendix A.

As denoted by the correspondent time dynamics, the first two extracted modes (Fig. A.5) exhibit a 12-month periodicity (panels c,f). Thus suggesting their association with precipitation patterns characterized by one annual minimum and maximum. Indeed, by observing the magnitude (panels a,d), it is possible to note that these modes are predominantly influential in regions with a tropical climate, featuring distinct wet and dry seasons where water variability is largely driven by precipitation. Also, the phases show the seasonally aligned regions participating to these modes (panels b,e). In DMD, some modes naturally appear as complex conjugate pairs due to applying the method to real-valued data, which leads to a real-valued linear operator. This operator captures oscillatory behavior through complex eigenvalues, with paired modes representing components of real-valued oscillations (Kutz et al., 2016). Modes 1 and 2 illustrate this well, as they encode the dominant oscillatory dynamics of the system. While these conjugate modes share the same magnitude and growth or decay rate, their phases differ—rotating in opposite directions in the complex plane—resulting in real-valued oscillations when combined.

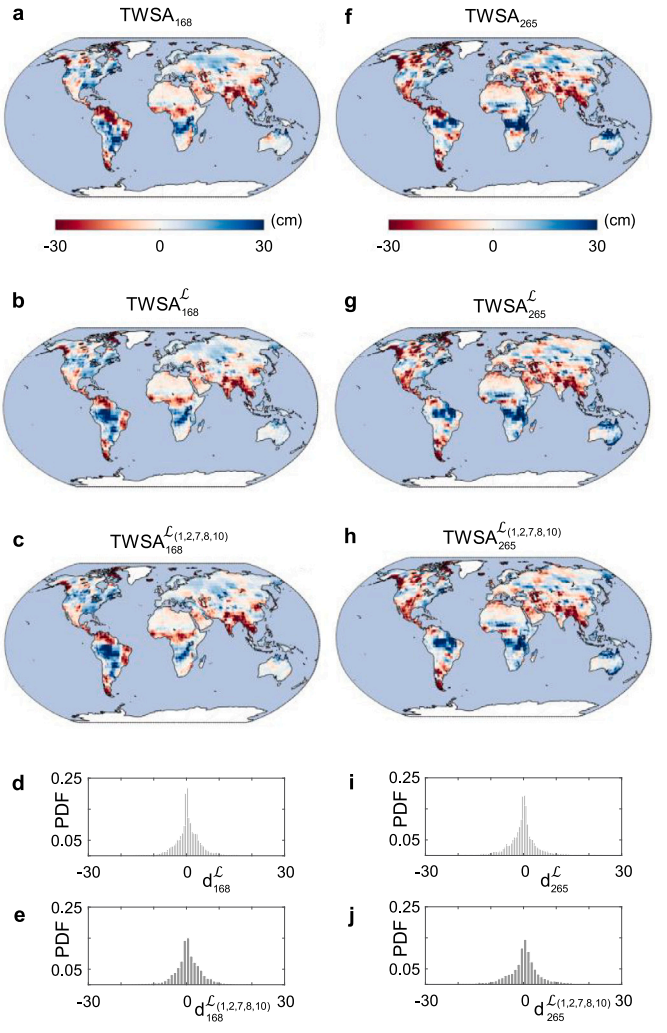

Fig. 1. (a) GRACE data at $t = 168$ (March 2016), TWSA_{168}, (b) correspondent model prediction, $\mathrm{TWSA}^{\mathcal{L}}_{168}$, and (c) contribution to the prediction given by a subset of modes $\mathrm{TWSA}^{\mathcal{L}_\alpha}_{168}$ with $\boldsymbol{\alpha} = (1, 2, 7, 8, 10)$. In (d) is the PDF of the differences $\mathrm{d}^{\mathcal{L}}_t$ between (b) and (a), while in (e) is the PDF of the differences $\mathrm{d}^{\mathcal{L}_\alpha}_t$ between (c) and (a). (f)–(j) are the same of (a)–(e) for $t = 265$ (April 2024).

The third and fourth modes (Fig. A.6) capture seasonal effects with a 4-year periodicity, marked by an increasing and decreasing amplitude, respectively, over the observation period. These are reasonably linked to complex ocean-atmosphere interactions determining natural climate patterns such as, e.g., El Niño and La Niña. The fifth and sixth modes (Fig. A.7) include an initial state of the system, which rapidly declines to zero after the baseline period. The seventh and eighth modes (Fig. A.8) encapsulate the trend effects in the data, with the latter contributing from approximately the midpoint of the observation period, while the former maintains a consistent influence throughout. These modes exhibit global contributions. Lastly, the ninth and tenth modes (Fig. A.9) denote a constant behavior and a periodic dynamic with a progressively increasing amplitude, characterized by two peaks and one minimum across the observation period, respectively.

We argue that specific spatiotemporal structures within the data are essential for defining the dynamics of TWSA. We show that by analyzing the spatial error distribution at two distinct time points, $t = 168$, which corresponds to March 2016, and $t = 265$ to April 2024. Specifically, we first demonstrate that the TWSA data (Fig. 1a,f)

are reproduced accurately by the complete DMD model obtained by considering the contribution of all modes. Hereinafter, we refer to this DMD model as $\mathrm{TWSA}^{\mathcal{L}}$ (Fig. 1b,g). Secondly, we show that comparable accuracy is achieved through DMD when we sum only the contribution of selected modes, i.e., $\mathrm{TWSA}^{\mathcal{L}_{\boldsymbol{\alpha}}}$ with $\boldsymbol{\alpha} = (1, 2, 7, 8, 10)$ indicating the subset of modes considered for the prediction, resulting in only minor discrepancies in data reproduction (Fig. 1c,h).

To quantify the error associated with the model predictions in both cases, we compute the vectors $\mathbf{d}_t^{\mathcal{L}}$ and $\mathbf{d}_t^{\mathcal{L}_{\boldsymbol{\alpha}}}$ as defined in Eq. (7). As such, for $t = 168$ and $t = 265$, we get two vectors of differences containing $N = 58\,908$ values each, one for each cell's grid located on a land area in the map. The probability distribution of these differences is described by the histograms for the two representation scenarios, i.e., reconstructions using all modes and those using only the most contributing modes (Fig. 1d,e, and i,j, respectively). The histograms are sensibly symmetric around zero, and the probability quickly decays to nearly zero for $|\mathrm{d}_t^{\mathcal{L}}| > 10$, indicating an appreciable degree of accuracy of the model.

After demonstrating the dominant influence of a selected subset of DMD spatiotemporal structures at two different time points, we expand on these initial findings by analyzing the average spatial contribution of each mode to the predicted TWSA over time, i.e. $\langle\, \mathrm{TWSA}_t^{\mathcal{L}_\alpha} \rangle$, where $\alpha = 1, 2, \ldots, 10$ indicates the mode (Fig. 2a). This analysis reveals that modes 1, 2, and 10 exhibit periodic contributions ranging from −2 cm to +2 cm. In contrast, modes 7 and 8 show a marked decline over time, with mode 8 decreasing more rapidly, reaching approximately −6 cm. The contributions of the remaining modes are characterized by an average spatial contribution of around zero.

To analyze the mode spatial influence beyond the averages and to explore, in particular, regions experiencing the most extreme values, we consider the contribution to the predicted TWSA of each mode separately and quantify the percentage of cells where this contribution is above and below ±10 cm over time (Fig. 2b–e). Fig. 2b–c highlights that the percentage of cells with values below −10 cm is significant for modes 7 and 8, with mode 8 becoming predominant in the last three years. This means that modes 7 and 8 reflect a diffuse global pattern intensifying over time, with an annual increase rate in the percentage of cells with values below −10 cm exceeding 3% for mode 8 and approximately 1% for mode 7 during the final years of the observation period (Fig. 2b). Similarly, Fig. 2d–e shows the percentage of cells with TWSA values exceeding +10 cm, which also becomes significant for modes 7 and 8. In this case, mode 8 shows an annual increase rate in the percentage of cells exceeding 2.5%, while mode 7 exhibits a rate of approximately 1% in the final years of the observation period. Mode 8's contribution becomes dominant in the last year (Fig. 2d).

To analyze the intensifying global pattern in the last years associated with trend-dominated modes, in Fig. 3, we indicate the areas exhibiting a contribution of mode 7 (panels a–c) and mode 8 (panels d–f) to the predicted TWSA values above and below ±10 cm, at time points $t = 217$, 241, and 265, corresponding to April in 2020, 2022, and 2024, respectively. Our analysis reveals where the progressive expansion of regions exceeding the specified thresholds occurs.

We observe that both modes 7 and 8 contribute to these patterns, often with opposing signs, with mode 8 becoming increasingly dominant over time, as corroborated by the results in Fig. 2b–c. This is particularly pronounced in regions such as northern Venezuela, central Argentina, Brazil, California, western Colombia and Colorado basins, the Mississippi Basin, and southern Mexico and Guatemala. A similar condition is observed in southeastern Africa, southwestern Russia, northern India, northeastern China, and northern and eastern Australia. Regions such as the Gulf of Alaska coast and the Patagonian ice fields exhibit combined effects from the two modes, which intensify the negative predicted TWSA values. In contrast, tropical western Africa shows an additive effect that increases the positive predicted TWSA values. New regions with spreading patterns linked to mode 8 have emerged, including Mexico, central-eastern Canada, northern Eurasia,

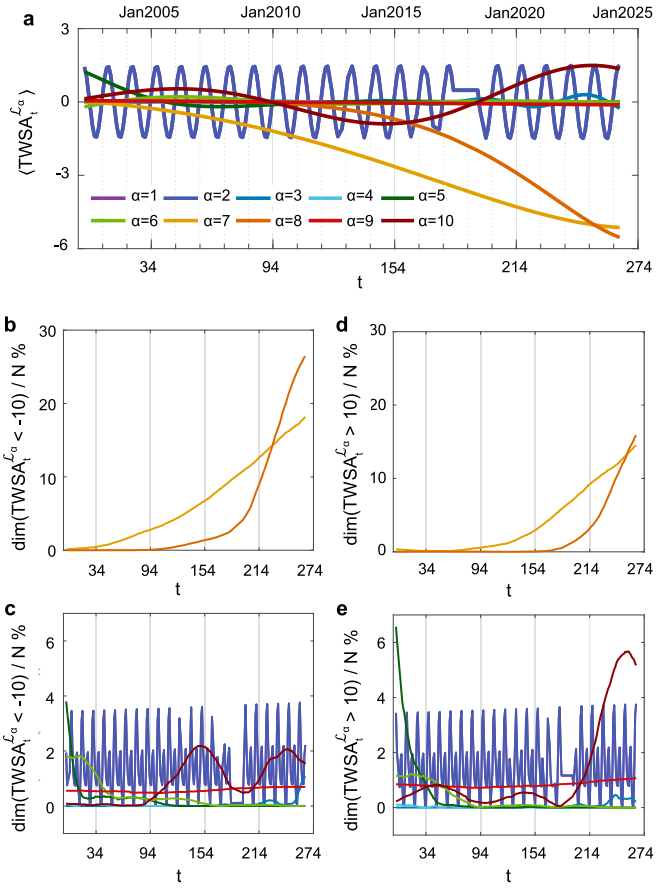

Fig. 2. (a) $\langle\, \mathrm{TWSA}_t^{\mathcal{L}_\alpha} \rangle$ (in cm) is the spatial average of the contribution of the αth mode to the optDMD prediction in time. Note that the time series for $\alpha = 1, 2$ overlap. In (b)–(c) is the % of cells with $\mathrm{TWSA}_t^{\mathcal{L}_\alpha} < -10$ cm. In (d)–(e) is the % of cells with $\mathrm{TWSA}_t^{\mathcal{L}_\alpha} > 10$ cm.

western China, and eastern Siberia. A comparable spatial expansion is observed for mode 7 in central-eastern Europe.

In Fig. 4 we analyze TWSA values provided by DMD over the last ten years of the observation period at $t = 145$, 205, and 265, which correspond to April 2014, 2019, and 2024, respectively. As before, this analysis focuses on regions where the predicted TWSA values exceed the defined thresholds ±10 cm. The goal is to quantify the contribution of trend-dominated modes compared to others as they increasingly become dominant. The first row illustrates the joint contribution of modes 7 and 8, i.e., $\mathrm{TWSA}^{\mathcal{L}_{(7,8)}}$, while the second one displays the effect of the remaining modes. The third row depicts the overall model prediction (considering all modes), i.e., $\mathrm{TWSA}^{\mathcal{L}}$, whose validation is provided in Appendix B Fig. B.10 against GRACE data. Finally, the last row of Fig. 4 proposes the percentage of the contribution of modes 7 and 8 over the overall prediction, i.e., it is computed as $\mathrm{TWSA}^{\mathcal{L}_{(7,8)}}/\mathrm{TWSA}^{\mathcal{L}} \cdot 100$. The selection of the three time points is based on the following criteria. We choose April in all cases since this month corresponds to the peak of the periodic contribution of modes 1 and 2 (Fig. 2a), thus facilitating also the comparison among the different years. As for the years, they correspond to a minimum, null, and maximum spatial average contribution of mode 10, respectively (Fig. 2a). In Appendix C the differences of the maps in the selected years are shown in Fig. C.11 to highlight the changes over time.

Upon analyzing panels a, e, and i, we notice an expansion of regions with $\mathrm{TWSA}^{\mathcal{L}_{(7,8)}}$ values exceeding +10 cm in areas such as Nile headwaters and tropical western Africa, northwestern and northern and eastern

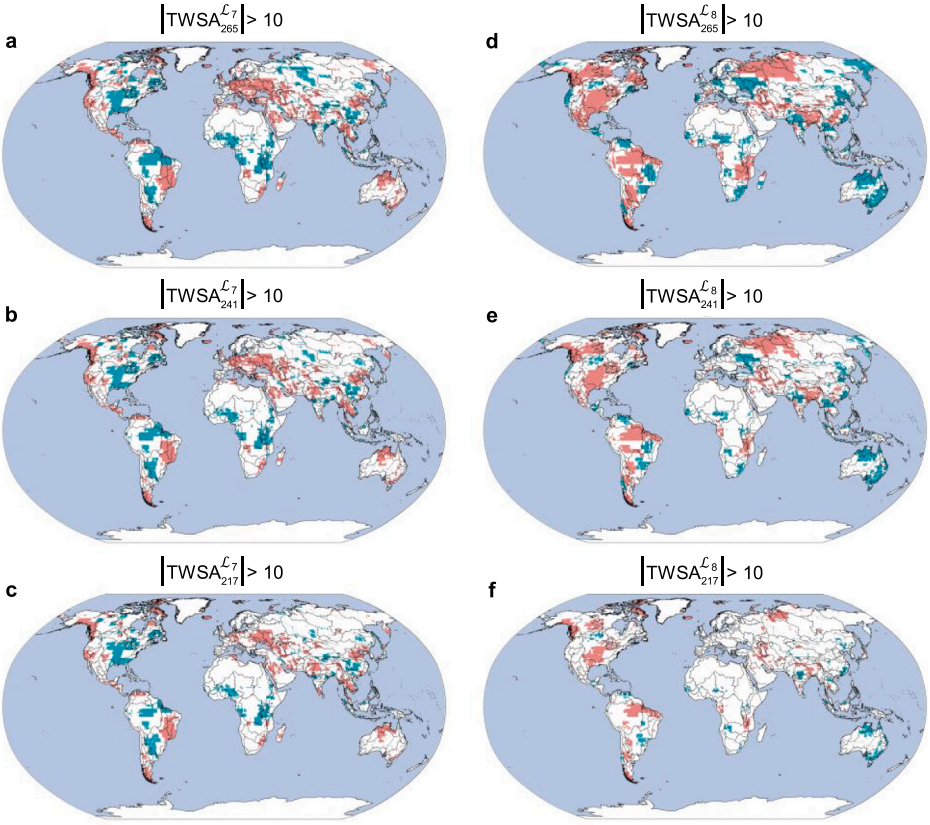

Fig. 3. (a)–(c) show the cells in which $\left|\mathrm{TWSA}_t^{\mathcal{L}_\alpha}\right| > 10$ cm (values < -10 cm are in red and >10 cm are in green), for $\alpha = 7$ and $t = 265, 241, 217$ (April 2024, 2022, 2020), respectively. (d)–(f) show the same for $\alpha = 8$.

Australia. However, the majority of expanding regions are associated with $\mathrm{TWSA}^{\mathcal{L}(7,8)}$ below −10 cm. In the Americas, these areas include the Patagonian ice fields, central Argentina, central Brazil, Mexico, the southern high plains and eastern Texas, the Gulf of Alaska coast, central Canada, and the Canadian Archipelago. Additionally, this pattern is noted in northern Africa, western Asia, northern and eastern India, and northern Eurasia (see Fig. C.11 first row for more details).

Focusing on panels b, f, and j, we observe that the contribution of the remaining modes, which is mainly driven by modes 1, 2, and 10 is displayed, as expected, in regions with a tropical climate, and also in the Gulf of Alaska coast. Areas emerge over time in the southern high plains and eastern Texas, and northern Eurasia, while an attenuation is detected in the north of Australia. We also observe an intensification of extreme TWSA values due to these modes over time (see Fig. C.11 second row for more details).

An analysis of the overall TWSA predictions, $\mathrm{TWSA}^{\mathcal{L}}$, at each time point (panels c, g, k) reveals a diffuse decrease in North and South America, western Asia, northern and eastern India, and northern Eurasia. This is mainly due to trend-dominated modes that exhibit an increasing weight over time, as quantified in panels d, h, and l, where the percentage of their contribution is shown. Table 1 lists the main areas exhibiting a relevant increase or decrease in TWSA over the selected time frame in compliance with the results shown in Fig. 4 and includes a comparison with findings referred to previous years of GRACE data in Rodell et al. (2018) (see Fig. C.11 third row for more details).

We observe that trend-dominated modes generally control TWSA values in the same areas previously classified as affected by climate change or human impact, while periodic modes are prevalent where natural variability was detected as a cause of change in TWSA values. DMD predictions confirm most trends detected in TWSA values in the earlier period, with few exceptions in areas affected by natural variability such as Brazil, Southeastern Africa, and Northwestern Australia. Overall, DMD demonstrates a high accuracy in analyzing space–time patterns in GRACE data. It effectively distinguishes between periodic components related to natural variability and trend components associated with human-induced changes, such as climate change and water depletion, within the selected time frame, providing valuable insights into critical TWSA dynamics at the global scale.

5. Conclusion

We apply DMD to TWSA derived from the GRACE missions to identify the dominant spatiotemporal patterns underlying total water storage dynamics. DMD enables decomposing the data into spatial modes with associated temporal behavior, providing a reduced-order representation that is physically interpretable and encapsulates the complex hydrological processes involved. The extracted spatiotemporal structures reveal key periodic and trend-driven components, offering insights into the underlying mechanisms driving water storage variability globally. Our results show that a small number of modes capture the majority of the variability in TWSA across diverse regions. DMD effectively separates trends from seasonal oscillations, enabling clearer attribution of storage changes to different hydrological processes. Our analysis shows that trend-dominated modes correspond to significant and accelerating changes in water storage, in areas affected by climate change and water depletion. These findings align with previous studies, reinforcing the effectiveness of DMD in capturing the governing mechanisms directly from the data and underscoring the need for sustained monitoring and mitigation efforts to address challenges related to water scarcity and climate resilience.

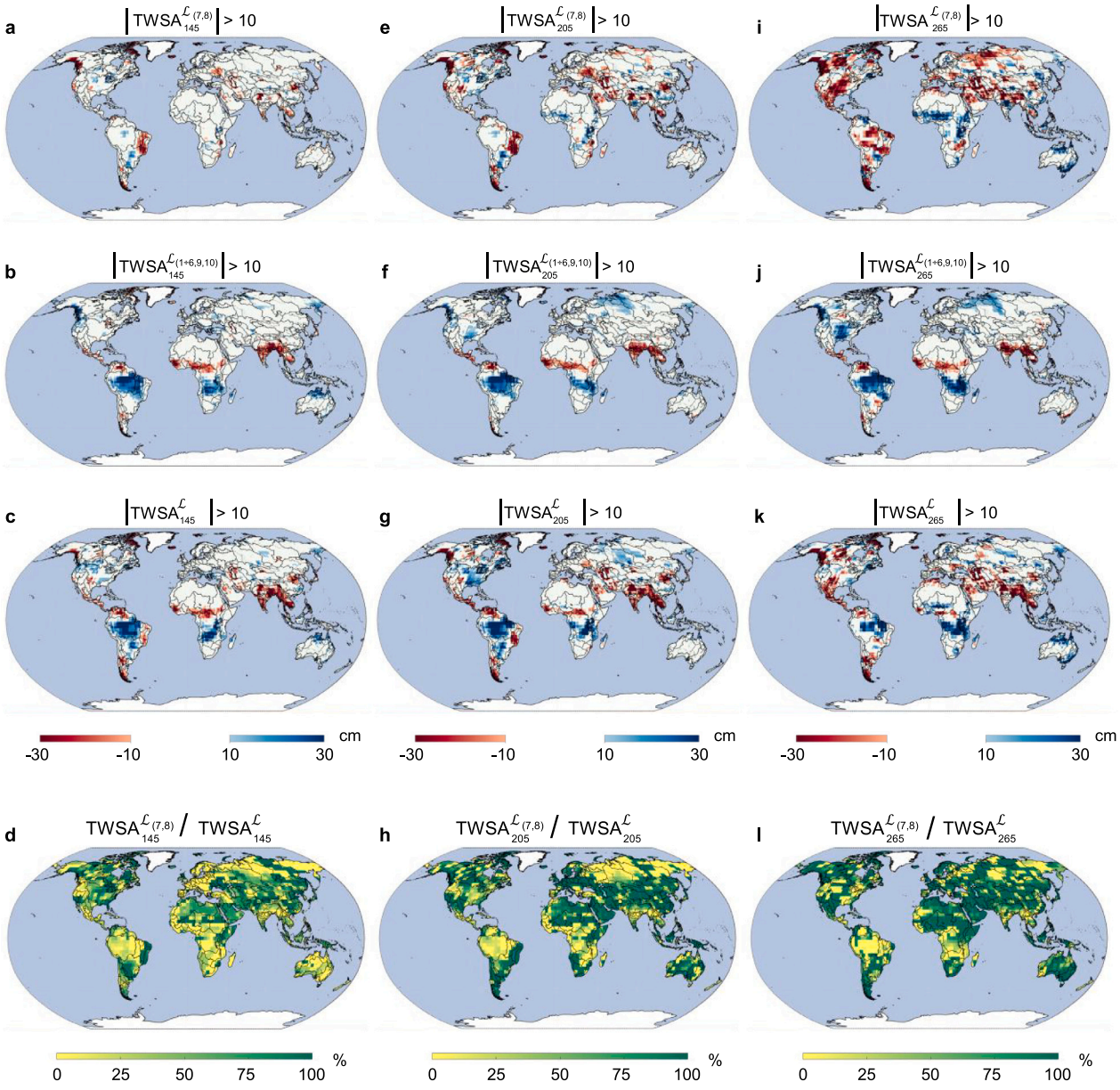

Fig. 4. TWSA (in cm) for the cells in which $\left|\mathrm{TWSA}_t^{\mathcal{L}_\alpha}\right| > 10$ cm for $t = 145$ (April 2014), and (a) $\alpha = (7,8)$, and (b) $\alpha = (1 \div 6, 9, 10)$. (c) shows the same when all the modes are used in the prediction, and (d) shows the percentage $\mathrm{TWSA}_{145}^{\mathcal{L}_{(7,8)}}/\mathrm{TWSA}_{145}^{\mathcal{L}} \cdot 100$. (e)–(h) show the same for $t = 205$ (April 2019), and (i)–(l) for $t = 265$ (April 2024).

CRediT authorship contribution statement

G. Libero: Writing – original draft, Methodology, Funding acquisition, Data curation, Conceptualization. **V. Ciriello:** Writing – review & editing, Supervision, Methodology, Funding acquisition, Conceptualization.

Declaration of competing interest

The authors declare that they have no known competing financial interests or personal relationships that could have appeared to influence the work reported in this paper.

Acknowledgments

The authors acknowledge GRACE/GRACE-FO Mascon data that are available at http://grace.jpl.nasa.gov. The authors acknowledge support from University of Bologna RFO (Ricerca Fondamentale Orientata) 2020–2021. GL acknowledges support from the Marco Polo mobility scholarship for research 2021 of the University of Bologna.

Appendix A. Modes and time dynamics

Here, Figs. A.5–A.9, show the magnitude of the modes (panels a,d), expressed in the same unit of TWSA data, i.e., cm, to quantify

Table 1
Characterization of the principal areas identified by Fig. 4.

Location	[Region] Trend, Cause identified by Rodell et al. (2018)	TWSA$^{\mathcal{L}}$ 2014–24	Dominant modes
North America			
Gulf of Alaska coast	[3] ↓ glaciers retreating	↓	Trend
Canadian Archipelago	[4] ↓ glacier and ice-cap loss	↓	Trend
Central Canada	[19] ↓ surface water drying	↓	Trend
Southern High Plains and eastern Texas	[22] ↓ drought	↓	Trend
Mexico	NA	↓	Trend
South America			
Patagonian ice fields	[23] ↓ ice-field melt	↓	Trend
Central Argentina	[24] ↓ from wet to dry period	↓	Trend
Central and western Brazil	[25] ↑ recovery from drought	↓	Periodic
Eastern Brazil	[26] ↓ recent drought	↑	Mixed
Eurasia			
Northern India	[7] ↓ groundwater depletion	↓	Trend
Central India	[8] ↑ precipitation increase	↑	Periodic
Tibetan Plateau	[10] ↑ precipitation increases	↑	Trend
Northwester China	[11] ↓ glacier melt, irrigated agriculture	↓	Trend
North China Plain	[12] ↓ groundwater depletion	↑	Trend
Eastern India Region	[13] ↓ water depletion, precip. decrease	↓	Mixed
Northwestern Saudi Arabia	[14] ↓ groundwater depletion	↓	Trend
Northern Middle East	[15] ↓ groundwater depletion, drought	↓	Mixed
Caspian Sea	[18] ↓ decline of the Caspian Sea	↓	Trend
Africa			
Okavango Delta	[27] ↑ from dry to wet period	↑	Periodic
Nile headwaters	[28] ↑ increasing lake levels, groundwater	↑	Mixed
Tropical western Africa	[29] ↑ precipitation increase	↑	Mixed
Northern Congo	[30] ↓ precipitation decrease	↑	Periodic
Southeastern Africa	[31] ↓ precipitation decrease	↑	Periodic
Northern Africa	[32] ↓ groundwater depletion	↓	Trend
Australia			
Northern and Eastern Australia	[33] ↑ from dry to wet period	↑	Mixed
Northwestern Australia	[34] ↓ return to normal after wet period	↑	Mixed

the contribution of specific spatial locations to that mode, the angle between the real and imaginary components (panels b,e) to describe the phase of each element relative to others oscillating at the frequency associated with the mode, and the time dynamics (panels c,f).

Appendix B. Error analysis

Here, in Fig. B.10, we provide validation of model predictions for the time points considered in the analysis, i.e., $t = 145, 205, 265$, by depicting TWSA data, on the first row, the difference between data and the prediction TWSA$^{\mathcal{L}}$, on the second row, and computing the PDF of $\mathbf{d}_t^{\mathcal{L}}$, on the third row, similarly to what we do in Fig. 1. As already observed for $t = 265$, the histograms are sensibly symmetric around zero, and the probability quickly decays to nearly zero for $|\mathrm{d}_t^{\mathcal{L}}| > 10$, indicating an appreciable degree of accuracy of the model, with local major discrepancies, more evident for late times, in some of the regions associated with higher TWSA values.

Appendix C. Analysis of variations

To highlight changes in TWSA values that occurred over time at the selected time points, considering the overall prediction TWSA$^{\mathcal{L}}$ and the specific contributions due only to trend-dominated modes and the remaining modes, here in Fig. C.11 we show the maps of the differences between $t = 265$ and $t = 205, 145$, in the first and second column, respectively. We observe that the main differences over time are associated with the joint contribution of modes 7 and 8 to the overall DMD prediction. This result is expected given the increasing impact of these two modes, which becomes prevalent in the last years of the observation period.

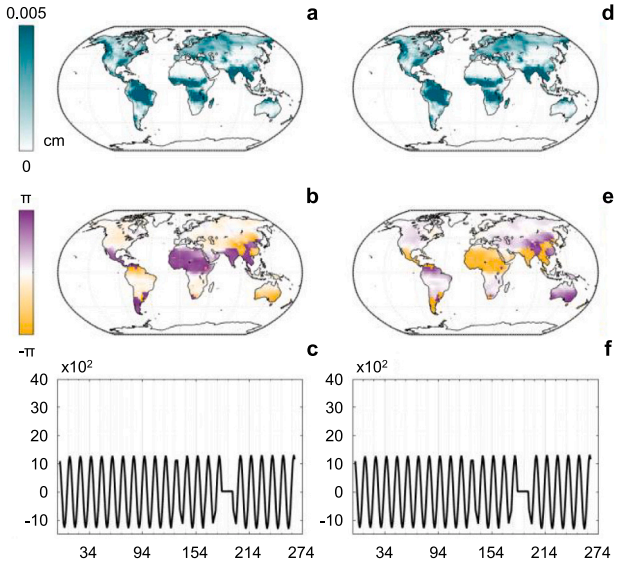

Fig. A.5. Dynamic Mode Decomposition of GRACE data via optDMD. (a)–(b) Show the magnitude and phase of mode 1, (c) the correspondent time dynamic; (d)–(f) do the same for mode 2.

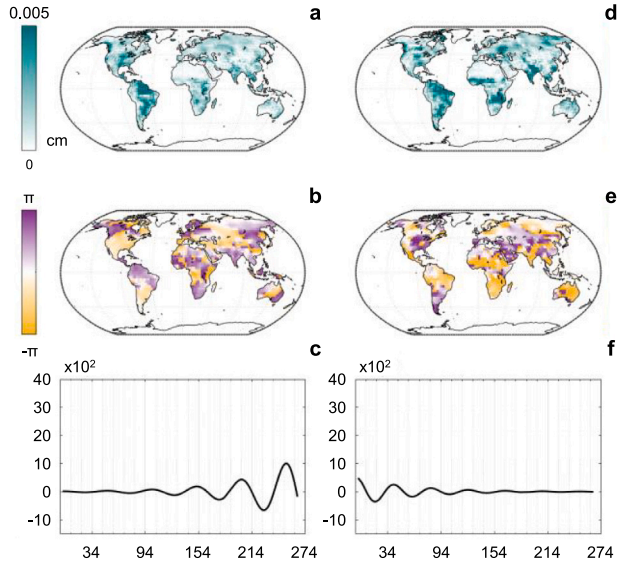

Fig. A.6. Dynamic Mode Decomposition of GRACE data via optDMD. (a)–(b) Show the magnitude and phase of mode 3, (c) the correspondent time dynamic; (d)–(f) do the same for mode 4.

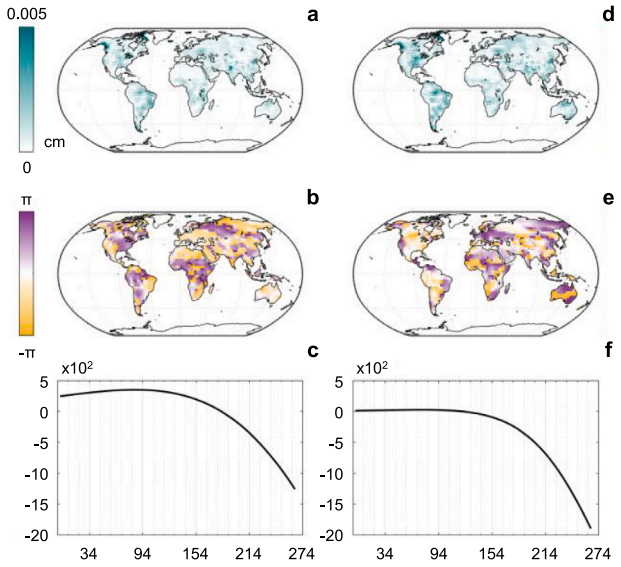

Fig. A.8. Dynamic Mode Decomposition of GRACE data via optDMD. (a)–(b) Show the magnitude and phase of mode 7, (c) the correspondent time dynamic; (d)–(f) do the same for mode 8.

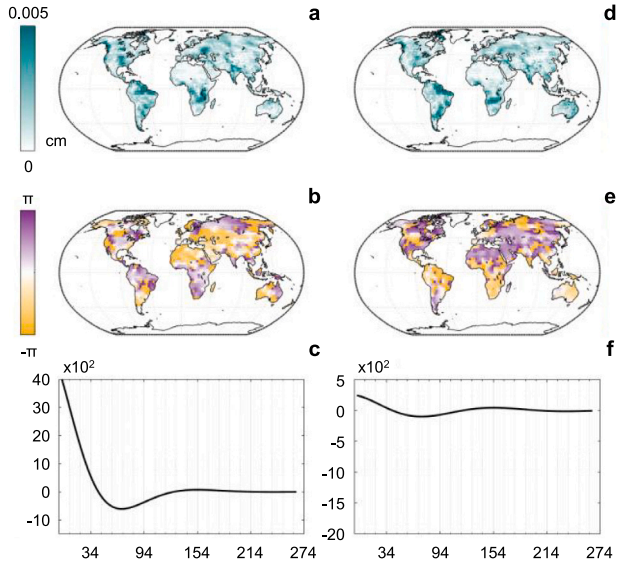

Fig. A.7. Dynamic Mode Decomposition of GRACE data via optDMD. (a)–(b) Show the magnitude and phase of mode 5, (c) the correspondent time dynamic; (d)–(f) do the same for mode 6.

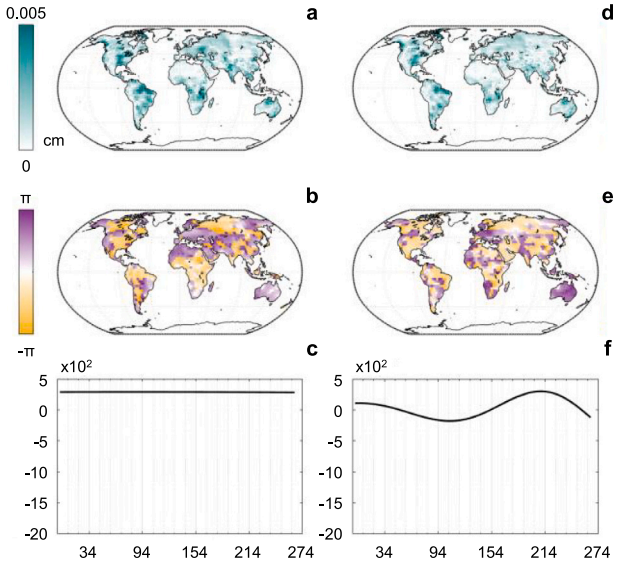

Fig. A.9. Dynamic Mode Decomposition of GRACE data via optDMD. (a)–(b) Show the magnitude and phase of mode 9, (c) the correspondent time dynamic; (d)–(f) do the same for mode 10.

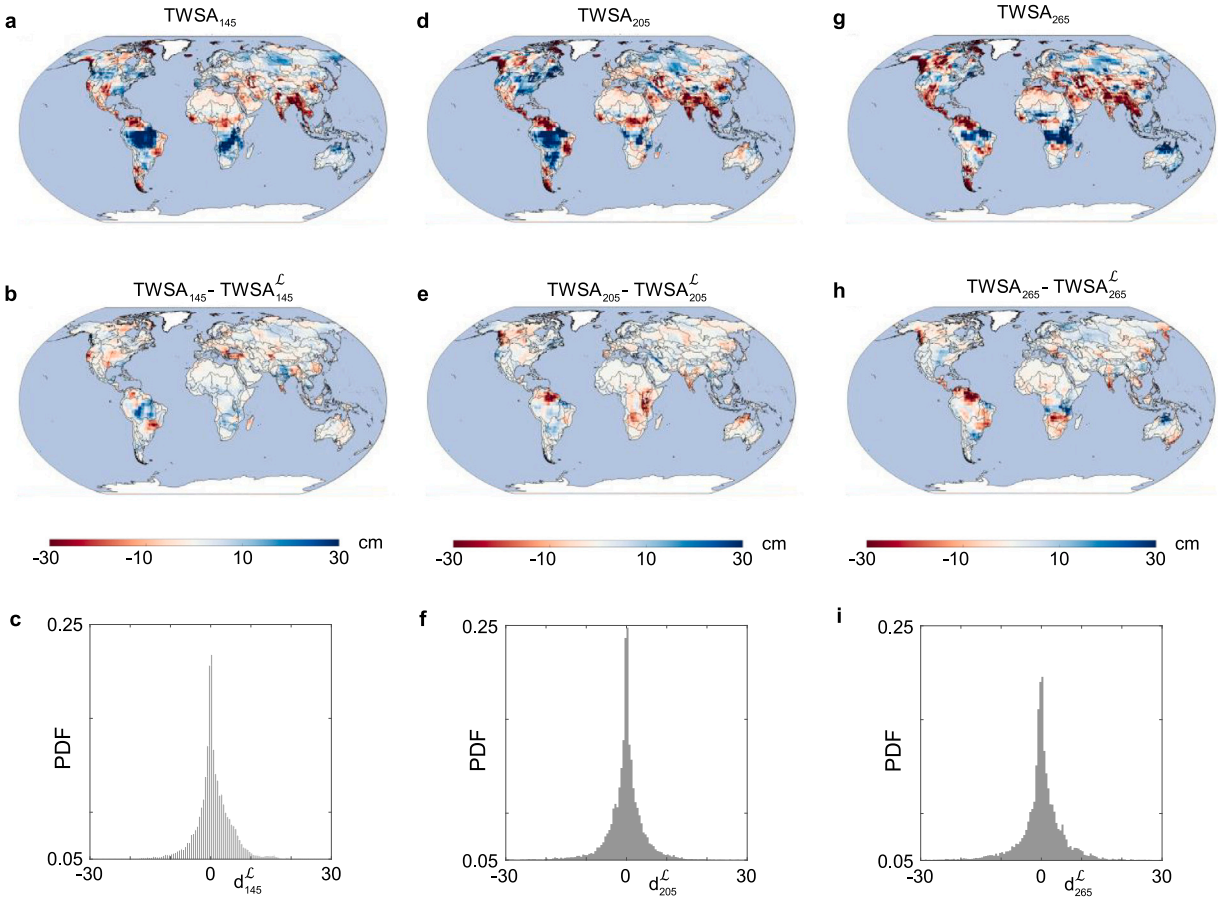

Fig. B.10. (a) GRACE data at $t = 145$ (April 2014), $TWSA_{145}$, (b) correspondent model prediction, $TWSA^{\mathcal{L}}_{145}$, and (c) PDF of the differences, $d^{\mathcal{L}}_{t}$, between (b) and (a). (d)–(f) and (g)–(i) show the same for $t = 205$ (April 2019), and $t = 265$ (April 2024), respectively.

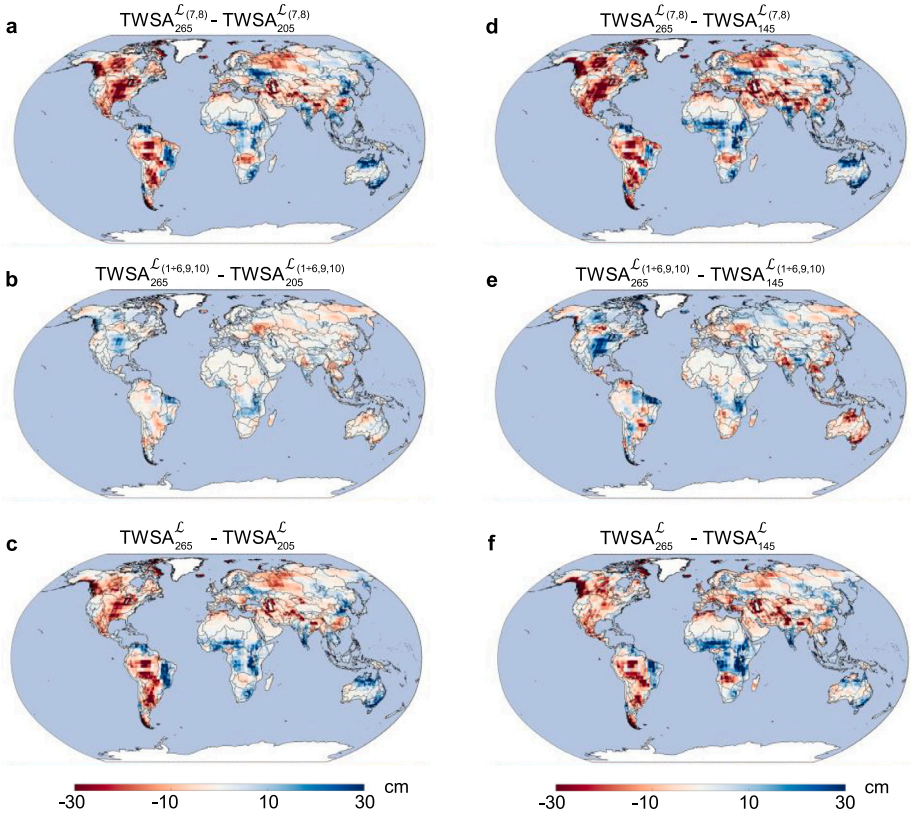

Fig. C.11. (a)–(c) show the differences between model predictions at times $t = 265$ (April 2024) and $t = 205$ (April 2019), when it is considered (a) only the contribution of modes 7 and 8, (b) only the contribution of the remaining modes, and (c) the contribution of all the modes. (d)–(f) show the same for the differences between model predictions at times $t = 265$ (April 2024) and $t = 145$ (April 2014).

Data availability

There are no data sharing issues since all of the numerical information is provided in the figures produced by solving the equations in the paper.

References

Askham, T., Kutz, J.N., 2018. Variable projection methods for an optimized dynamic mode decomposition. SIAM J. Appl. Dyn. Syst. 17 (1), 380–416. http://dx.doi.org/10.1137/m1124176.

Bagheri, S., 2014. Effects of weak noise on oscillating flows: Linking quality factor, floquet modes, and Koopman spectrum. Phys. Fluids 26 (9), http://dx.doi.org/10.1063/1.4895898.

Castle, S.L., Thomas, B.F., Reager, J.T., Rodell, M., Swenson, S.C., Famiglietti, J.S., 2014. Groundwater depletion during drought threatens future water security of the Colorado River Basin. Geophys. Res. Lett. 41 (16), 5904–5911. http://dx.doi.org/10.1002/2014gl061055.

Dawson, S.T.M., Hemati, M.S., Williams, M.O., Rowley, C.W., 2016. Characterizing and correcting for the effect of sensor noise in the dynamic mode decomposition. Exp. Fluids 57 (3), http://dx.doi.org/10.1007/s00348-016-2127-7.

de Graaf, I.E.M., Gleeson, T., (Rens) van Beek, L.P.H., Sutanudjaja, E.H., Bierkens, M.F.P., 2019. Environmental flow limits to global groundwater pumping. Nature 574 (7776), 90–94. http://dx.doi.org/10.1038/s41586-019-1594-4.

Duke, D., Soria, J., Honnery, D., 2011. An error analysis of the dynamic mode decomposition. Exp. Fluids 52 (2), 529–542. http://dx.doi.org/10.1007/s00348-011-1235-7.

Famiglietti, J.S., Lo, M., Ho, S.L., Bethune, J., Anderson, K.J., Syed, T.H., Swenson, S.C., de Linage, C.R., Rodell, M., 2011. Satellites measure recent rates of groundwater depletion in California's central valley. Geophys. Res. Lett. 38 (3), http://dx.doi.org/10.1029/2010gl046442.

Frappart, F., Papa, F., Güntner, A., Tomasella, J., Pfeffer, J., Ramillien, G., Emilio, T., Schietti, J., Seoane, L., da Silva Carvalho, J., Medeiros Moreira, D., Bonnet, M.-P., Seyler, F., 2019. The spatio-temporal variability of groundwater storage in the amazon river basin. Adv. Water Resour. 124, 41–52. http://dx.doi.org/10.1016/j.advwatres.2018.12.005.

Hemati, M.S., Rowley, C.W., Deem, E.A., Cattafesta, L.N., 2017. De-biasing the dynamic mode decomposition for applied Koopman spectral analysis of noisy datasets. Theor. Comput. Fluid Dyn. 31 (4), 349–368. http://dx.doi.org/10.1007/s00162-017-0432-2.

Huggins, X., Gleeson, T., Kummu, M., Zipper, S.C., Wada, Y., Troy, T.J., Famiglietti, J.S., 2022. Hotspots for social and ecological impacts from freshwater stress and storage loss. Nat. Commun. 13 (1), http://dx.doi.org/10.1038/s41467-022-28029-w.

Kutz, J.N., Brunton, S.L., Brunton, B.W., Proctor, J.L., 2016. Dynamic Mode Decomposition. Society for Industrial and Applied Mathematics, http://dx.doi.org/10.1137/1.9781611974508.

Landerer, F.W., Flechtner, F.M., Save, H., Webb, F.H., Bandikova, T., Bertiger, W.I., Bettadpur, S.V., Byun, S.H., Dahle, C., Dobslaw, H., Fahnestock, E., Harvey, N., Kang, Z., Kruizinga, G.L.H., Loomis, B.D., McCullough, C., Murböck, M., Nagel, P., Paik, M., Pie, N., Poole, S., Strekalov, D., Tamisiea, M.E., Wang, F., Watkins, M.M., Wen, H.-Y., Wiese, D.N., Yuan, D.-N., 2020. Extending the global mass change data record: Grace follow-on instrument and science data performance. Geophys. Res. Lett. 47 (12), http://dx.doi.org/10.1029/2020gl088306.

Libero, G., Chiofalo, A., Ciriello, V., Tartakovsky, D.M., 2024a. Extended dynamic mode decomposition for model reduction in fluid dynamics simulations. Phys. Fluids 36 (6), http://dx.doi.org/10.1063/5.0207957.

Libero, G., Ciriello, V., Tartakovsky, D., 2024b. Dynamic mode decomposition of GRACE satellite data. Adv. Water Resour. 193, 104834. http://dx.doi.org/10.1016/j.advwatres.2024.104834.

Libero, G., Tartakovsky, D., Ciriello, V., 2024c. Polynomial chaos enhanced by dynamic mode decomposition for order-reduction of dynamic models. Adv. Water Resour. 186, 104677. http://dx.doi.org/10.1016/j.advwatres.2024.104677.

Lu, H., Tartakovsky, D.M., 2020. Lagrangian dynamic mode decomposition for construction of reduced-order models of advection-dominated phenomena. J. Comput. Phys. 407, 109229. http://dx.doi.org/10.1016/j.jcp.2020.109229.

Lu, H., Tartakovsky, D.M., 2021. Extended dynamic mode decomposition for inhomogeneous problems. J. Comput. Phys. 444, 110550. http://dx.doi.org/10.1016/j.jcp.2021.110550.

Mezić, I., 2013. Analysis of fluid flows via spectral properties of the Koopman operator. Annu. Rev. Fluid Mech. 45 (Volume 45, 2013), 357–378. http://dx.doi.org/10.1146/annurev-fluid-011212-140652, URL: https://www.annualreviews.org/content/journals/10.1146/annurev-fluid-011212-140652.

NASA/JPL, 2023. JPL GRACE and GRACE-FO mascon ocean, ice, and hydrology equivalent water Height Coastal resolution improvement (CRI) filtered release 06.1 version 03. http://dx.doi.org/10.5067/TEMSC-3JC63.

Rodell, M., Famiglietti, J.S., Wiese, D.N., Reager, J.T., Beaudoing, H.K., Landerer, F.W., Lo, M.-H., 2018. Emerging trends in global freshwater availability. Nature 557 (7707), 651–659. http://dx.doi.org/10.1038/s41586-018-0123-1.

Rodell, M., Reager, J.T., 2023. Water cycle science enabled by the GRACE and GRACE-FO satellite missions. Nat. Water 1 (1), 47–59. http://dx.doi.org/10.1038/s44221-022-00005-0.

Rowley, C.W., Mezić, I., Bagheri, S., Schlatter, P., Henningson, D.S., 2009. Spectral analysis of nonlinear flows. J. Fluid Mech. 641, 115–127. http://dx.doi.org/10.1017/s0022112009992059.

Sashidhar, D., Kutz, J.N., 2022. Bagging, optimized dynamic mode decomposition for robust, stable forecasting with spatial and temporal uncertainty quantification. Philos. Trans. R. Soc. A: Math. Phys. Eng. Sci. 380 (2229), http://dx.doi.org/10.1098/rsta.2021.0199.

Scanlon, B.R., Fakhreddine, S., Rateb, A., de Graaf, I., Famiglietti, J., Gleeson, T., Grafton, R.Q., Jobbagy, E., Kebede, S., Kolusu, S.R., Konikow, L.F., Long, D., Mekonnen, M., Schmied, H.M., Mukherjee, A., MacDonald, A., Reedy, R.C., Shamsudduha, M., Simmons, C.T., Sun, A., Taylor, R.G., Villholth, K.G., Vörösmarty, C.J., Zheng, C., 2023. Global water resources and the role of groundwater in a resilient water future. Nat. Rev. Earth Environ. 4 (2), 87–101. http://dx.doi.org/10.1038/s43017-022-00378-6.

Schmid, P.J., 2010. Dynamic mode decomposition of numerical and experimental data. J. Fluid Mech. 656, 5–28. http://dx.doi.org/10.1017/s0022112010001217.

Stampoulis, D., Reager, J.T., David, C.H., Andreadis, K.M., Famiglietti, J.S., Farr, T.G., Trangsrud, A.R., Basilio, R.R., Sabo, J.L., Osterman, G.B., Lundgren, P.R., Liu, Z., 2019. Model-data fusion of hydrologic simulations and GRACE terrestrial water storage observations to estimate changes in water table depth. Adv. Water Resour. 128, 13–27. http://dx.doi.org/10.1016/j.advwatres.2019.04.004.

Tapley, B.D., Bettadpur, S., Ries, J.C., Thompson, P.F., Watkins, M.M., 2004. GRACE measurements of mass variability in the earth system. Science 305 (5683), 503–505. http://dx.doi.org/10.1126/science.1099192.

Tapley, B.D., Watkins, M.M., Flechtner, F., Reigber, C., Bettadpur, S., Rodell, M., Sasgen, I., Famiglietti, J.S., Landerer, F.W., Chambers, D.P., Reager, J.T., Gardner, A.S., Save, H., Ivins, E.R., Swenson, S.C., Boening, C., Dahle, C., Wiese, D.N., Dobslaw, H., Tamisiea, M.E., Velicogna, I., 2019. Contributions of GRACE to understanding climate change. Nat. Clim. Chang. 9 (5), 358–369. http://dx.doi.org/10.1038/s41558-019-0456-2.

Tu, J.H., Rowley, C.W., Luchtenburg, D.M., Brunton, S.L., Kutz, J.N., 2014. On dynamic mode decomposition: Theory and applications. J. Comput. Dyn. 1 (2), 391–421. http://dx.doi.org/10.3934/jcd.2014.1.391.

Watkins, M.M., Wiese, D.N., Yuan, D.-N., Boening, C., Landerer, F.W., 2015. Improved methods for observing earth's time variable mass distribution with GRACE using spherical cap mascons. J. Geophys. Res.: Solid Earth 120 (4), 2648–2671. http://dx.doi.org/10.1002/2014jb011547.

Wiese, D.N., Landerer, F.W., Watkins, M.M., 2016. Quantifying and reducing leakage errors in the JPL RL05M GRACE mascon solution. Water Resour. Res. 52 (9), 7490–7502. http://dx.doi.org/10.1002/2016wr019344.